

# Phase projection errors in rf-driven optically pumped magnetometers

Zoran D. Grujić,<sup>1</sup> Marija Ćurčić,<sup>2</sup> Aleksandra Kocić,<sup>2</sup> Antoine Weis,<sup>3</sup> and Theo Scholtes<sup>4,\*</sup>

<sup>1</sup>*Institute of Physics Belgrade, University of Belgrade, Serbia*<sup>†</sup>

<sup>2</sup>*Institute of Physics Belgrade, University of Belgrade, Serbia*

<sup>3</sup>*Physics Department, University of Fribourg, Chemin du Musée 3, CH-1700 Fribourg, Switzerland*

<sup>4</sup>*Leibniz Institute of Photonic Technology, Albert-Einstein-Strasse 9, D-07745 Jena, Germany*

(Dated: October 1, 2024)

We study the phase between the oscillating (rf) excitation field and the detected (light) power modulation in scalar rf-driven optically pumped magnetometers (OPMs), in particular in the  $M_x$  configuration. While the static dependence of the demodulation phase on the direction of the external static magnetic field vector can be largely overcome by aligning the oscillating rf field along the light propagation direction, we show that a dynamic (transient) phase response can appear under tilts of the magnetic field. We analytically solve the corresponding modified Bloch equation and obtain agreement with experimental observations in an  $M_x$  magnetometer setup using a paraffin-coated Cs vapor cell. The results reveal fundamental limitations of  $M_x$  magnetometers in terms of response time and accuracy, in particular when operated with active electronic feedback, e.g., using a phase-locked loop. Thus, the work is highly relevant in important magnetometry applications, where the direction of the quasi-static magnetic field of interest is not known *a priori* and/or not constant over time, or in measurements, in which a large detection bandwidth is paramount. Such conditions are encountered, e.g., in geomagnetic surveying, in particular with mobile platforms.

## I. INTRODUCTION

Optically pumped magnetometers (OPM) represent the most sensitive non-cryogenic type of magnetic field sensor available today [1]. With their exquisite performance they are vital in applications where extremely small changes in the magnetic field need to be detected or monitored, e.g., in magnetocardiography [2–5], magnetoencephalography [6, 7], fundamental physics experiments [8, 9], geomagnetic prospection [10, 11], detection and imaging of magnetic nanoparticles [12–14], exploration of magnetic fields in space [15–17], and many more, as recently reviewed, e.g., in [18].

OPMs are based on a variety of magneto-optical effects in (alkali-metal) vapors [19] and exist in a wide range of different implementations, as they can be tailored very well to the intended application.

When it comes to operation within the geomagnetic field, the so-called  $M_x$  magnetometer has a very long tradition and is proven to be a good choice both in terms of sensitivity and robustness [2, 20–25]. In this type of OPM, the modulus  $B_0$  of the static magnetic field vector  $\vec{B}_0$  is inferred from the driven Larmor precession frequency,  $\omega_L = \gamma_F B_0$ , of an ensemble of gaseous polarized atomic spins, typically enclosed into a vapor cell (for  $^{133}\text{Cs}$  used here,  $\gamma_F/2\pi \approx 3.5 \text{ Hz/nT}$ ). The Larmor precession is 'driven' by an additionally applied weak magnetic field oscillating at  $\omega_{\text{rf}}$  near the Larmor frequency. In the standard  $M_x$  magnetometer a single circularly polarized, light beam propagating along  $\vec{k}$  and tuned resonantly to an atomic transition (typically the  $D_1$  and

$D_2$  lines in alkali atoms) is used for both, the creation of atomic spin polarization by a process called optical pumping [26], and the read-out of the spin precession signal. As the light beam is transmitted through the vapor cell, it acquires a modulation at the rf field frequency that can be detected by a photo diode placed behind the cell. The amplitude of light modulation shows a resonant behavior when rf field frequency and Larmor frequency coincide, as does the phase between rf field and detected light intensity modulation. The steady-state solution for the phase signal, which is typically recorded using a lock-in amplifier (cp. Sec. III A), in dependence on the rf detuning  $\delta\omega = \omega_{\text{rf}} - \omega_L$  has the form [27]

$$\varphi(\delta\omega) = \varphi^0 - \arctan \frac{\delta\omega}{\gamma}, \quad (1)$$

where  $\gamma$  is the spin relaxation rate. When  $\omega_{\text{rf}}$  is fixed, a change in the modulus of the static magnetic field  $|\vec{B}_0|$  will lead to a change in  $\delta\omega$ , thus in  $\varphi$ . For small changes in the magnetic field modulus, viz. deviations in  $\delta\omega$  small compared to  $\gamma$ , the sensor response is linear and can be used to monitor field changes in the so-called 'free-running mode'. However, to track changes in the Larmor frequency which are larger than the resonance linewidth, commonly an active feedback is employed. Due to the arctan-dependence, its property of being less affected by technical noise compared to in-phase, quadrature and magnitude lock-in signals, and the strong suppression of rf broadening [28], the phase signal is the natural choice for  $M_x$  sensor operation using such active feedback loop. Here, typically the feedback acts on  $\omega_{\text{rf}}$  to keep  $\varphi$  at its set value, where commonly  $\varphi^0$  is chosen as working point of the PI(D) controller where the signal slope is maximized. This mode of operation is often referred to as 'phase locked loop' (PLL) and can not only increase the dynamic range of the sensor, but can also

\* theo.scholtes@leibniz-ipt.de

† zoran.grujic@ipb.ac.rs

increase the measurement bandwidth [29]. However, for both methods described above to work satisfactorily, the offset phase  $\varphi^0$  needs to be extremely well under control. Disregarding electronic phase shifts [30], the offset phase  $\varphi^0$  depends on the orientation of  $\vec{B}_{\text{rf}}$  and  $\vec{B}_0$  with respect to the light propagation direction  $\vec{k}$ . In the classical  $M_x$  magnetometer implementation [2, 20–23], where  $\vec{B}_{\text{rf}} \perp \vec{k}$ , the offset phase is given by

$$\varphi_{\perp}^0 = \arctan(\cos \alpha \cot \phi), \quad (2)$$

where  $\alpha$  is the angle between  $\vec{B}_0$  and  $\vec{k}$  and  $\phi$  is the angle between  $\vec{B}_{\text{rf}}$  and the projection of  $\vec{B}_0$  into the plane perpendicular to  $\vec{k}$  [27]. Consequently, a change in direction of  $\vec{B}_0$  does in general lead to a change in  $\varphi_{\perp}^0$ , thus to a change in  $\varphi$ . Thus, when the phase signal is used within an active feedback stabilizing  $\varphi$ , a change in direction of  $\vec{B}_0$  can mimic a change in the magnitude of  $\vec{B}_0$ , leading to an erroneous feedback on  $\omega_{\text{rf}}$ . We term this effect 'static phase projection error' (SPPE). So, in this configuration the feedback loop can only operate well, if the direction of  $\vec{B}_0$  stays constant over time with respect to  $\vec{k}$  and  $\vec{B}_{\text{rf}}$ .

When we adjust the sensor geometry to have  $\vec{B}_{\text{rf}} \parallel \vec{k}$ , it was shown in [27], that the offset phase is constant for all angles  $\alpha$  and  $\phi$ , except for a flip by  $\pi$  in transition between the two half spaces with either  $\vec{k}$  parallel or anti-parallel to the projection of  $\vec{B}_0$ , respectively,

$$\varphi_{\parallel}^0 = -\frac{\pi}{2} \text{sign}(\cos \alpha). \quad (3)$$

As the offset phase  $\varphi_{\parallel}^0$  is constant over one entire half space, no phase change should occur when the  $\vec{B}_0$  direction changes within the respective half space. Thus, this configuration has been referred to as the *true-scalar magnetometer* (TSM) [29].

In this paper we show, that Eq. 3 is true only in the steady state approximation in which it was derived. In the general case, when  $\vec{B}_0$  changes direction, a transient change of the phase is observed, which, after a time interval scaling with  $\gamma$ , settles back to the expected steady-state value. We term this effect dynamic phase projection error (DPPE) and its understanding is the motivation of this work. The nature of DPPE depends strongly on the respective direction of the  $\vec{B}_0$  rotation where two cases can be distinguished: rotation within the plane spanned by  $\vec{B}_0$  and  $\vec{k}$  and rotation of  $\vec{B}_0$  out of this plane. As we show below, in the later case a residual phase shift appears even if averaged over a full or multiple rf cycles (as typically done in lock-in detection).

The outline of the paper is as follows: In Sec. II we solve the equation of motion for the spin orientation vector to obtain analytical expressions in the resonant case ( $\delta\omega = 0$ ), reproducing the DPPE phenomenon. In Sec. III we detail on the experiments we did to demonstrate the effect and show the experimental results in agreement with model expectations. Finally, we discuss implications of the effect in  $M_x$  magnetometers within

real-world applications in Sec. IV and conclude the paper in Sec. V.

## II. THEORY

We extend previous work by Weis et al. [29] to solve the modified Bloch equation in the case  $\vec{B}_{\text{rf}} \parallel \vec{k}$  (TSM) including the transient evolution of the spin orientation vector and derive equations describing the signals detected by a lock-in amplifier in the experiment. We give the analytical solution for the case of resonant rf magnetic field ( $\delta\omega = 0$ ).

We set up the modified Bloch equation in the laboratory frame, solve it in the rotating frame using the rotating frame approximation (RWA), transform the solution back into the laboratory frame, and obtain the lock-in signals. Finally, based on those solutions, in order to analyse the DPPE, we consider rotations around the  $x$ - and  $y$ -axis, respectively.

### A. The Bloch equation

The equation of motion we consider here is the Bloch equation [31] extended to cover optical pumping [29]. It describes the evolution of the atomic spin orientation vector  $\vec{S}(t)$  under interaction with the magnetic field  $\vec{\Omega}(t) = \gamma_F \vec{B}(t)$  and resonant circularly polarized light propagating along  $\vec{k}$ , resulting in optical pumping at a rate  $\gamma_p$ :

$$\dot{\vec{S}}(t) = \vec{S}(t) \times \vec{\Omega}(t) - \gamma \vec{S}(t) + \gamma_p (\vec{k} - \vec{S}(t)). \quad (4)$$

The first term  $\vec{S}(t) \times \vec{\Omega}(t)$  describes the torque of the total magnetic field exerted on  $\vec{S}$  where

$$\vec{\Omega}(t) = \vec{\Omega}_L + \vec{\Omega}_{\text{rf}}(t) \quad (5)$$

$$= \gamma_F (\vec{B}_0 + \vec{B}_{\text{rf}}(t)). \quad (6)$$

The constant  $\gamma_F$  is the gyromagnetic ratio,  $\vec{\Omega}_L = \gamma_F \vec{B}_0$  the angular Larmor frequency, where  $\vec{B}_0$  is the static magnetic field and  $\vec{B}_{\text{rf}}(t)$  the oscillating magnetic field

$$2\vec{\Omega}_{\text{rf}}(t) = 2\vec{\Omega}_{\text{rf}} \sin(\omega_{\text{rf}}t) \quad (7)$$

$$= \gamma_F \vec{B}_{\text{rf}}(t) \quad (8)$$

$$= \gamma_F \vec{B}_{\text{rf}} \sin(\omega_{\text{rf}}t). \quad (9)$$

The optical pumping rate  $\gamma_p$  gives rise to the creation of the spin orientation in direction of laser beam propagation direction  $\vec{k}$ . Please note that  $|\vec{k}| = 1$  and  $|\vec{S}(t)| \leq 1$ , so that the pumping process acts towards a build up of maximal atomic spin orientation parallel to  $\vec{k}$ , counteracted by the spin relaxation. For simplicity, we assume isotropic relaxation of  $\vec{S}$  that can be expressed as scalar

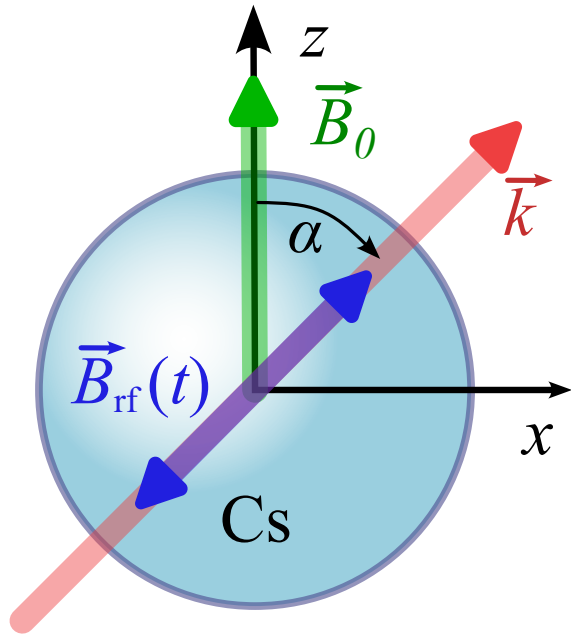


FIG. 1. Geometry of the true scalar magnetometer (TSM). The static magnetic field  $\vec{B}_0$  is in  $z$ -direction,  $\vec{k}$  lies in  $zx$ -plane and is at angle  $\alpha$  to  $\vec{B}_0$ . The rf magnetic field  $\vec{B}_{\text{rf}}(t)$  oscillates in parallel to  $\vec{k}$ .

relaxation rate  $\gamma$  and is related to spin relaxation processes like collisions of atoms with the cell wall or other atoms or molecules in the cell [32].

### B. TSM geometry

The geometry of the TSM is fully defined by two vectors:  $\vec{\Omega}_L = (0, 0, \omega_L)^\top$ , where  $\omega_L = \gamma_F |\vec{B}_0|$ , and  $\vec{k} \parallel \vec{\Omega}_{\text{rf}}$ , where  $\vec{\Omega}_{\text{rf}} = \Omega_{\text{rf}} (\sin \alpha, 0, \cos \alpha)^\top$ . For convenience we chose the magnetic field to point in direction of the  $z$ -axis, while  $\vec{k}$  lies in the  $zx$ -plane, tilted by an angle  $\alpha$  with respect to  $z$ , see Fig. 1. The optimal performance of the  $M_x$  magnetometer in terms of sensitivity is achieved at  $\alpha \approx 45^\circ$ . Please note, that such a definition is valid for any orientation of the magnetic field, i.e. if the direction of the magnetic field is not parallel to  $z$  axis, the coordinate system can be suitably rotated to have the magnetic field along the  $z$ -axis and  $\vec{k} \parallel \vec{B}_{\text{rf}}$  in  $zx$ -plane, where an equivalent TSM magnetometer is obtained, eventually with a different angle  $\alpha$ .

### C. Rotating wave approximation (RWA)

To solve the Bloch equation we transform into the rotating frame (rotating at  $\omega_{\text{rf}}$  in the clockwise (cw) direction), apply the rotating wave approximation, and transform back the solution into the laboratory frame. As

the spin orientation does precess around the  $z$ -axis, we choose  $z$  as our rotation axis. For simplicity, we choose  $\omega_L = \omega_{\text{rf}}$ . In this case, the static magnetic field vanishes in the rotating frame,  $\vec{\Omega}_L^{\text{R}} = (0, 0, 0)^\top$ . We use superscript 'R' to mark quantities in the rotating frame, and label the axes in the rotating frame as  $\hat{x}$ ,  $\hat{y}$  and  $\hat{z}$ . We can split  $\vec{\Omega}_{\text{rf}}$  into two components, one in  $z$ -direction which can be disregarded (its time average is zero), and the second in  $x$ -direction can be split in two counter-rotating components:

$$\begin{aligned} \text{cw} &\rightarrow \Omega_{\text{rf}} (\sin(\omega_{\text{rf}} t), +\cos(\omega_{\text{rf}} t), 0)^\top \sin \alpha, \\ \text{ccw} &\rightarrow \Omega_{\text{rf}} (\sin(\omega_{\text{rf}} t), -\cos(\omega_{\text{rf}} t), 0)^\top \sin \alpha. \end{aligned} \quad (10)$$

Now, the essence of the RWA is to disregard components rotating in the opposite direction of the spin, as they have lower impact than the co-rotating one. The resulting contribution is at frequency of  $2\omega_{\text{rf}}$ , which is far off-resonance and so its impact can be neglected here. For a more detailed discussion we refer the reader to [29]. As  $\vec{\Omega}_L^{\text{R}}$  vanishes, the remaining cw component of the total magnetic field in the rotating frame is equal to the projected rf magnetic field,

$$\vec{\Omega}^{\text{R}} = \vec{\Omega}_{\text{rf}}^{\text{R}} = \Omega_{\text{rf}} \begin{pmatrix} 0 \\ \sin \alpha \\ 0 \end{pmatrix}. \quad (12)$$

Similarly,  $\vec{k}$  is decomposed into a fixed component parallel to  $z$ , and the component along the  $x$ -direction. In the rotating frame the  $x$ -component of  $\vec{k}^{\text{R}}$  is not static, it rotates in the  $\hat{x}\hat{y}$ -plane and generates spin orientation in all directions perpendicular to  $\hat{z}$ . This does average to zero, and we can write

$$\vec{k}^{\text{R}} = \begin{pmatrix} 0 \\ 0 \\ \cos \alpha \end{pmatrix}. \quad (13)$$

Finally, the equation of motion in the rotating frame is

$$\begin{aligned} \dot{\vec{S}}^{\text{R}}(t) &= \vec{S}^{\text{R}}(t) \times \vec{\Omega}^{\text{R}} - \gamma \vec{S}^{\text{R}}(t) + \gamma_{\text{p}} (\vec{k}^{\text{R}} - \vec{S}^{\text{R}}(t)) \\ \dot{\vec{S}}^{\text{R}}(t) &= \vec{S}^{\text{R}}(t) \times \Omega_{\text{rf}} \begin{pmatrix} 0 \\ \sin \alpha \\ 0 \end{pmatrix} - \gamma \vec{S}^{\text{R}}(t) \\ &\quad + \gamma_{\text{p}} \left( \begin{pmatrix} 0 \\ 0 \\ \cos \alpha \end{pmatrix} - \vec{S}^{\text{R}}(t) \right). \end{aligned} \quad (15)$$

As this equation is free from time-dependent coefficients, we can solve it analytically.

### D. Analytic solution

Equation 15 is solved using *Wolfram Mathematica* [33] assuming  $0 < \alpha < \pi/2$ , and setting the initial condition

to be

$$\vec{S}^R(0) = \vec{S}(0) = \begin{pmatrix} S_x^0 \\ S_y^0 \\ S_z^0 \end{pmatrix}. \quad (16)$$

We split the solution into stationary  $\vec{S}^{\text{RS}}$  and transient  $\vec{S}^{\text{RT}}(t)$  parts:  $\vec{S}^R(t) = \vec{S}^{\text{RS}} + \vec{S}^{\text{RT}}(t)$ , with

$$\vec{S}^{\text{RS}} = \gamma_p \mathcal{L} \begin{pmatrix} -\Omega_{\text{rf}} \sin(2\alpha) \\ 0 \\ 2\gamma_{\text{tot}} \cos(\alpha) \end{pmatrix} \text{ and} \quad (17)$$

$$\vec{S}^{\text{RT}}(t) = e^{-\gamma_{\text{tot}} t} \begin{pmatrix} S_x^{\text{RT}}(t) \\ S_y^{\text{RT}}(t) \\ S_z^{\text{RT}}(t) \end{pmatrix}, \text{ with} \quad (18)$$

$$S_x^{\text{RT}}(t) = [S_x^0 + 2\mathcal{L}\gamma_p G_{\text{rf}} \cos(\alpha)] \cos(G_{\text{rf}} t) \\ + [-S_z^0 + 2\mathcal{L}\gamma_p \gamma_{\text{tot}} \cos(\alpha)] \sin(G_{\text{rf}} t), \quad (19)$$

$$S_y^{\text{RT}}(t) = S_y^0, \quad (20)$$

$$S_z^{\text{RT}}(t) = [S_z^0 - 2\mathcal{L}\gamma_p \gamma_{\text{tot}} \cos(\alpha)] \cos(G_{\text{rf}} t) \\ + [S_x^0 + 2\mathcal{L}\gamma_p G_{\text{rf}} \cos(\alpha)] \sin(G_{\text{rf}} t), \quad (21)$$

where we substituted

$$\gamma_{\text{tot}} = \gamma + \gamma_p, \quad (22)$$

$$G_{\text{rf}} = \Omega_{\text{rf}} \sin(\alpha), \quad (23)$$

$$\mathcal{L} = \frac{1}{2} \frac{1}{\gamma_{\text{tot}}^2 + G_{\text{rf}}^2}. \quad (24)$$

Please note here, that the stationary solution  $\vec{S}^{\text{RS}}$  is not a function of time: If we use  $\vec{S}^{\text{RS}}$  as initial condition then the system will not have to evolve towards the steady state as it is already there.

The spin orientation in the laboratory frame  $\vec{S}^L(t)$  is obtained after multiplying the solution in the rotating frame by the inverse of the rotation matrix we used to switch into the rotating frame,

$$\vec{S}^L(t) = R_z^{-1}(\omega_{\text{rf}} t + \phi) \vec{S}^R(t), \quad (25)$$

$$R_z^{-1}(\omega_{\text{rf}} t + \phi) = \begin{pmatrix} \cos(\omega_{\text{rf}} t + \phi) & \sin(\omega_{\text{rf}} t + \phi) & 0 \\ -\sin(\omega_{\text{rf}} t + \phi) & \cos(\omega_{\text{rf}} t + \phi) & 0 \\ 0 & 0 & 1 \end{pmatrix}, \quad (26)$$

where the superscript 'L' marks the laboratory frame.

One will notice the additional phase  $\phi$  we added to describe ambiguity between projection of  $\vec{k}^R$  onto the  $xy$ -plane and  $\vec{\Omega}^R$ . This is a consequence of the approximation introduced in Eq. 13. Also, the rf field will get the same phase in the laboratory frame,

$$2\vec{\Omega}_{\text{rf}}^L(t) = \gamma_F \vec{B}_{\text{rf}} \sin(\omega_{\text{rf}} t + \phi). \quad (27)$$

### E. Lock-in signals

In the first order approximation of Lambert-Beer law, the detected signal in the laboratory frame  $s(t)$  is pro-

portional to the scalar product of  $\vec{k}$  and  $\vec{S}^L(t)$  [34],

$$s(t) = \vec{k} \cdot \vec{S}^L(t). \quad (28)$$

We decompose the signal  $s(t)$  into in-phase ( $X$ ) and in-quadrature ( $Y$ ) components by grouping parts associated with  $\sin(\omega_{\text{rf}} t + \phi)$  and  $\cos(\omega_{\text{rf}} t + \phi)$ ,

$$s(t) = (X^S + X^T) \sin(\omega_{\text{rf}} t + \phi) \\ + (Y^S + Y^T) \cos(\omega_{\text{rf}} t + \phi), \quad (29)$$

and obtain

$$X^S = 0, \quad (30)$$

$$Y^S = -\gamma_p \mathcal{L} G_{\text{rf}} \sin(2\alpha), \quad (31)$$

$$X^T = S_y^0 \sin(\alpha) e^{-\gamma_{\text{tot}} t}, \quad (32)$$

$$Y^T = \sin(\alpha) [\cos(G_{\text{rf}} t) (S_x^0 + 2\mathcal{L}\gamma_p G_{\text{rf}} \cos \alpha) \\ + \sin(G_{\text{rf}} t) (2\mathcal{L}\gamma_p \gamma_{\text{tot}} \cos \alpha - S_z^0)] e^{-\gamma_{\text{tot}} t}, \quad (33)$$

where the superscripts 'S' and 'T' label static and transient parts, respectively. The DC offset of the signal is disregarded as it is irrelevant for future discussion.

The signal's phase  $\varphi$  can be expressed as arctan of the ratio between quadrature ( $Y$ ) and in-phase ( $X$ ) signals. Here, a special attention needs to be taken regarding the sign of both  $X$  and  $Y$ , defining the quadrant of point  $(X, Y)$ . In the general case the function `atan2` or `arctan2` (as defined in most programming languages like Fortran, Python, etc.) can be used to take care about the quadrants by always returning the correct value by the definition

$$\arctan2(y, x) = \begin{cases} \arctan \frac{y}{x} & x > 0 \\ \frac{\pi}{2} - \arctan \frac{x}{y} & y > 0 \\ -\frac{\pi}{2} - \arctan \frac{x}{y} & y < 0 \text{ (our case)} \\ \arctan \frac{y}{x} \pm \pi & x < 0 \\ \text{undefined} & x = 0 \text{ and } y = 0 \end{cases} \quad (34)$$

As  $Y < 0$  in our case, the phase signal  $\varphi(t)$ , measured by a lock-in amplifier, can be written as

$$\varphi(t) = -\frac{\pi}{2} - \arctan \left( \frac{X^S + X^T}{Y^S + Y^T} \right), \quad (35) \\ = -\frac{\pi}{2} - \arctan \left( \frac{S_y^0 e^{-\gamma_{\text{tot}} t}}{S_x^{\text{RT}}(t) e^{-\gamma_{\text{tot}} t} - 2\gamma_p \mathcal{L} G_{\text{rf}} \cos \alpha} \right) \quad (36)$$

The phase  $\varphi(t)$  is equal to  $-\pi/2$  in the steady state

$$\vec{S}^L(t \rightarrow \infty) = R_z^{-1}(\omega_{\text{rf}} t + \phi) \vec{S}^{\text{RS}}. \quad (37)$$

### F. The Dynamic Phase Projection Error

If we turn on our TSM at  $t = -\infty$  in a constant magnetic field,  $\vec{B}_0 \neq \vec{B}_0(t)$ , at  $t = 0$  we will find it to be in the steady state

$$\vec{S}(0) = R_z(\phi) \vec{S}^{\text{RS}}, \quad (38)$$



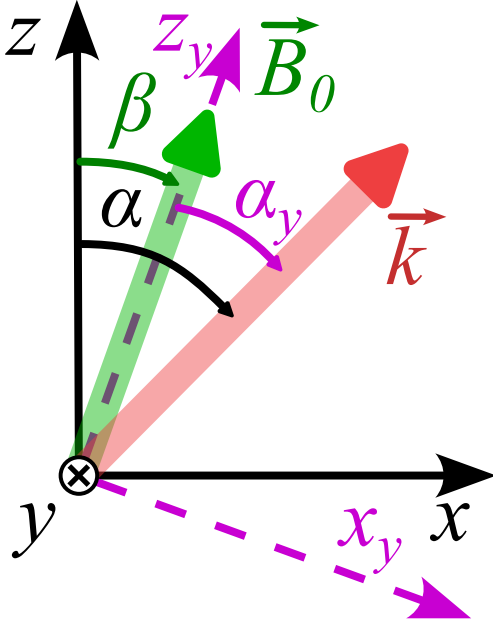


FIG. 2. Transformation in case of rotation around the  $y$ -axis.

see Eqs. 17 and 37. In case of a change in the modulus of the magnetic field  $|\vec{B}_0(t)|$ , the Larmor frequency will change instantaneously, and  $\varphi$  will change correspondingly, representing the difference between the new Larmor frequency  $\omega_L$  and the set rf frequency  $\omega_{\text{rf}}$  according to Eq. 1 [29].

However, now we analyze the case when the modulus remains constant,  $|\vec{B}_0(t)| = \text{const}$ , while the direction of  $\vec{B}_0(t)$  changes. In such a case,  $\varphi$  of a TSM should not change, but, as we show here, may undergo an unexpected transient evolution, before settling back to its

original, expected steady-state value of  $\varphi = -\pi/2$ .

If a rotation around the  $x$ - or the  $y$ -axis by an angle  $\beta$ , represented by rotation matrix  $R_{x,y}(\beta)$ , is applied to  $\vec{B}_0$  at  $t = 0$ , the geometry of the TSM will change. As a consequence, its relation to the  $\vec{S}^0$  will be different and it may not be the steady state of the modified TSM any more.

Let us consider a rotation around  $y$ -axis as presented in Fig. 2. The atomic spin will now be precessing in a plane orthogonal to the new vector of the magnetic field. This will be our new  $z_y$ -axis and the spin will be precessing in  $x_y y$ -plane. In this new coordinate system, defined by  $x_z, y, z_y$ , the TSM will operate without further modifications, except for the slightly changed  $\alpha$  and modified initial conditions. Consequently, we have

$$\alpha_y = \alpha - \beta, \quad (39)$$

$$\vec{S}_y(0) = R_y^{-1}(\beta) \vec{S}(0). \quad (40)$$

The  $x$ -rotation case is more complex, and the transformation will be performed in two steps, as indicated in Fig. 3. First, by  $x$ -rotation we obtain a  $x'y'z'$ -coordinate system, but as vector  $\vec{k}$  is not in the  $xz'$ -plane, the model we developed for TSM cannot be applied, cf. Fig. 3 a). In the next step we perform a rotation around the  $z'$ -axis by a suitable angle  $\theta$  so that  $\vec{k}$  appears to be in  $x_x z_x$ -plane, see Fig. 3 b). The detailed description of the transformation is:

$$\alpha_x = \arccos(\cos \alpha \cos \beta) \approx \alpha, \quad (41)$$

$$\theta = \text{sgn}(\beta) \arccos \frac{\sin \alpha}{\sqrt{\sin^2 \alpha + \cos^2 \alpha \sin^2 \beta}}, \quad (42)$$

$$\theta \approx \beta \cot \alpha, \quad (43)$$

$$\vec{S}_x(0) = R_{z'}^{-1}(\theta) R_x^{-1}(\beta) \vec{S}(0), \quad (44)$$

including the approximation for  $\theta$  for a small rotation angle  $\beta$ . After some math we obtain

$$\vec{S}_x(0) = 2\gamma_p \mathcal{L} \cos \alpha \begin{pmatrix} \gamma_{\text{tot}} \sin \phi \sin \beta - G_{\text{rf}} (\cos \beta \sin^2 \phi + \cos^2 \phi) \\ \cos \phi [G_{\text{rf}} (\cos \beta - 1) - \gamma_{\text{tot}} \sin \beta] \\ \gamma_{\text{tot}} \cos \beta + G_{\text{rf}} \sin \phi \sin \beta \end{pmatrix}, \quad (45)$$

$$\vec{S}_y(0) = 2\gamma_p \mathcal{L} \cos \alpha \begin{pmatrix} \gamma_{\text{tot}} \cos \phi \sin \beta - G_{\text{rf}} (\sin^2 \phi + \cos \beta \cos^2 \phi) \\ \sin \phi [G_{\text{rf}} (1 - \cos \beta) \cos \phi + \gamma_{\text{tot}} \sin \beta] \\ \gamma_{\text{tot}} \cos \beta + G_{\text{rf}} \cos \phi \sin \beta \end{pmatrix}. \quad (46)$$

By taking Eq. 45 and 46 as initial conditions for the phase calculation in Eq. 36, we obtain cumbersome expressions allowing very limited insight and not being suitable for presentation. Luckily, the first order approximation for small angle  $\beta$  leads to a very compact and

insightful form:

$$\varphi_x(t) = -\frac{\pi}{2} + a_x e^{-\gamma_{\text{tot}} t}, \quad (47)$$

$$\varphi_y(t) = -\frac{\pi}{2} + a_y e^{-\gamma_{\text{tot}} t}, \quad (48)$$

$$a_x = \theta + \beta \frac{\gamma_{\text{tot}}}{G_{\text{rf}}} \cos \phi, \quad (49)$$

$$a_y = -\beta \frac{\gamma_{\text{tot}}}{G_{\text{rf}}} \sin \phi. \quad (50)$$

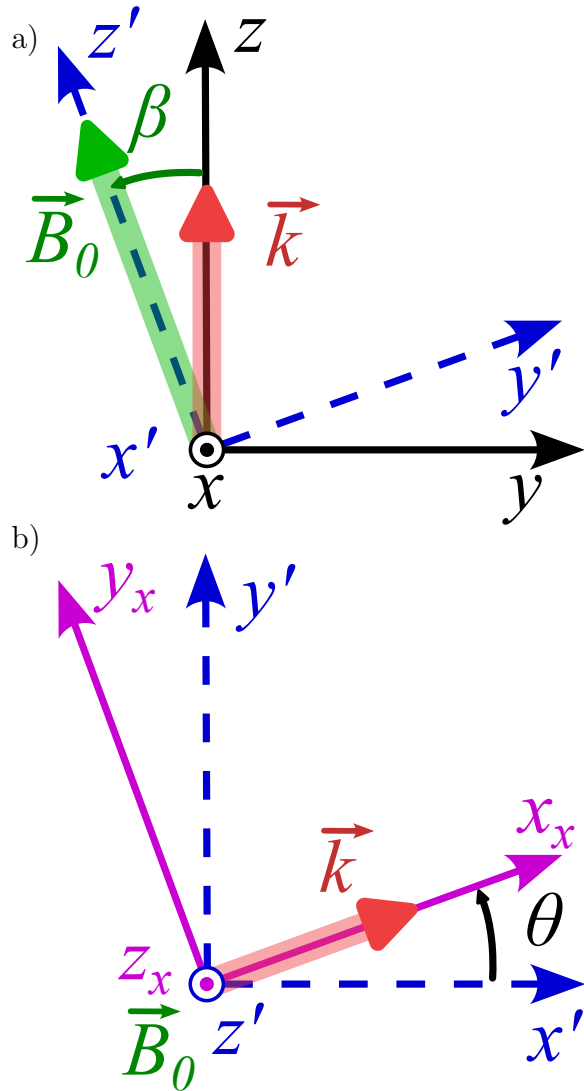


FIG. 3. Transformation in case of rotation around the  $x$ -axis.

At this point we learn that the TSM is not truly scalar on timescales defined by  $\gamma_{\text{tot}}$ . There is an evolution from one steady state to a new steady state in a slightly changed TSM geometry. The main difference in between the two rotations considered is in a fact that in case of the  $y$ -rotation, in certain cases, if we average the phase  $\varphi$  over  $\phi \in [0, 2\pi]$  we obtain no shift, while in other case the shift is  $\theta$ :

$$\bar{\varphi}_x = -\frac{\pi}{2} + \theta, \quad (51)$$

$$\bar{\varphi}_y = -\frac{\pi}{2}. \quad (52)$$

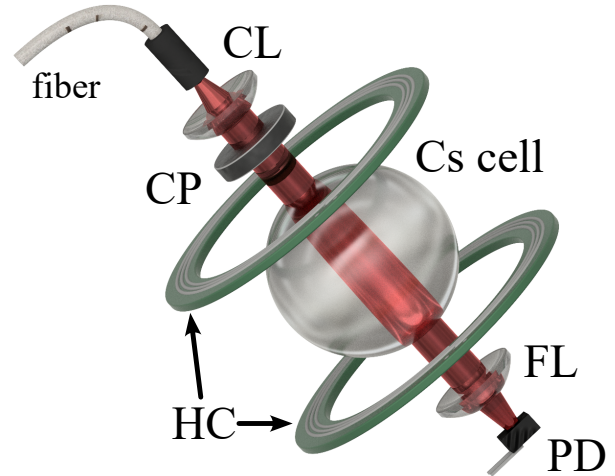


FIG. 4. Design of the TSM magnetometer head. We show its main parts while the plastic construction that holds all in its place is not shown. Please refer to the main text for details.

### III. EXPERIMENT

#### A. Experimental setup

For our TSM sensor head we employ a spherical  $^{133}\text{Cs}$  vapor cell with 28 mm diameter without buffer gas, and an inner anti-relaxation paraffin coating. The cell is at room-temperature, has side arm serving as Cs reservoir, and features an intrinsic relaxation rate of  $\approx 3$  Hz [35]. A special plastic mount made by 3D-printing encloses the cell, holds fiber coupler, optical elements, photo diode, and the Helmholtz coils (HC), made from printed-circuit board (50 mm diameter, 25 mm separation, 6 windings each), to apply the rf magnetic field  $\vec{B}_{\text{rf}}$  in parallel to  $\vec{k}$ , see Fig. 4. Amplitude and frequency of  $\vec{B}_{\text{rf}}$  are controlled by a lock-in amplifier (*Zurich Instruments*, model *HF2LI*). We find that the optimal TSM sensitivity is obtained when the lock-in output set to 400 mV amplitude is connected over 27 k $\Omega$  serial resistor to the HC, leading to  $G_{\text{rf}} = 2\pi 3.95$  rad/s. The same signal is used as reference for lock-in demodulation. Narrow-band ( $\delta\nu_1 \leq 5$  MHz) laser light at 894.6 nm from a tunable diode laser system (*Toptica Photonics*, model *DL pro*) is delivered by a multi-mode fiber, collimated by a lens (CL), then circularly polarized by a custom-made circular polarizer (CP). While traversing through the cell the laser light performs optical pumping of the Cs vapor and its intensity is being modulated by the precessing spin orientation  $\vec{S}(t)$  driven by  $\vec{B}_{\text{rf}}$ . The cell-transmitted light is focused by a second lens (FL) and detected by a photo diode (PD). For optimal sensitivity, the angle between laser beam propagation direction  $k$  and static magnetic field  $\vec{B}_0$  was set to be approximately 45°. The photo current generated in the PD is converted into voltage by a transimpedance amplifier (*Femto Messtechnik*,

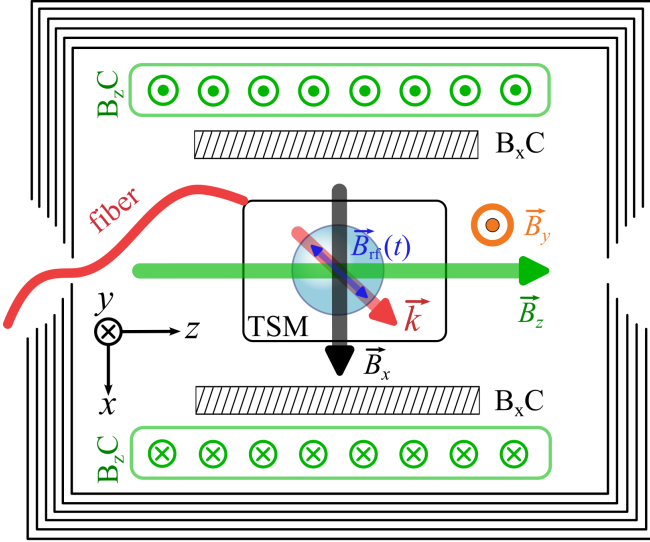


FIG. 5. Scheme of the experimental setup. A detailed picture of the TSM head is shown in Fig. 4. The magnetic field has been generated by a triaxial coil system, in Helmholtz configuration. The cylindrical coil to generate  $B_z$  has 15 windings, and a diameter of 220 mm. For modulating fields,  $B_x$  and  $B_y$ , the square coils of side dimensions of  $d_x = 150$  mm and  $d_y = 170$  mm, with 15 windings each, have been used.

model *DLPCA-200*) and demodulated by the lock-in amplifier.

The TSM sensor head is placed inside of a cylindrical six-layer  $\mu$ -metal magnetic shielding, see Fig. 5. A static field  $|\vec{B}_z| = 1.90 \mu\text{T}$  is applied along  $z$  using a solenoid driven by a low-noise current source (*Koheron*, model *DRV300-A-10*) at 9.19 mA. The required additional fields  $\vec{B}_{x,y}$  are produced by pairs of Helmholtz coils located inside the solenoid. We made sure to place the Cs vapor cell in center volume of all coils, where the magnetic field homogeneity is maximized. In order to rotate  $\vec{B}_0$  without changing the modulus of the field  $|\vec{B}_0|$ , we apply a 50% duty-cycle square-wave to the respective additional coil, i.e., for tipping  $\vec{B}_0$  within the  $xz$ -plane (around  $y$ ), the current through the  $\vec{B}_x$ -coil is applied as a bipolar square-wave function. In this way, in the positive semi-period the total field is  $\vec{B}_0 = (B_x, 0, B_z)^\top$  and in the negative semi-period it is  $(-B_x, 0, B_z)^\top$ , both with the same modulus  $\sqrt{B_x^2 + B_z^2}$ . We developed a special trigger circuit to synchronize the moment when tipping occurs with specified phase of the  $\vec{B}_{\text{rf}}$ . This allowed direct measurement of the  $\phi$  dependence as expected from Eqs. 47 and 48.

We observe the steady-state phase signal and tune the DC offset current through the  $B_x$ -coil to compensate remnant field components along the  $x$ -direction. The same procedure is applied for tipping  $\vec{B}_0$  within the  $yz$ -plane (around  $x$ ) using the  $B_y$ -coil instead.

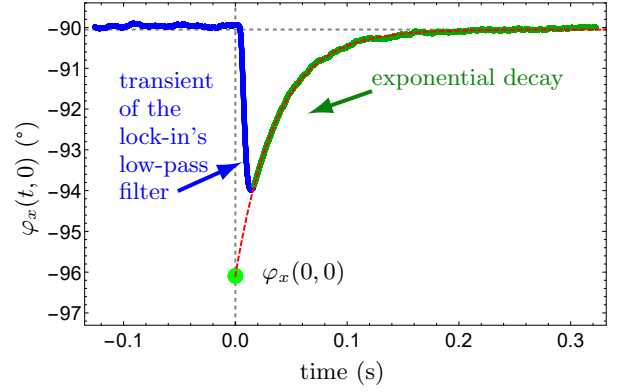


FIG. 6. Observed phase  $\varphi_x(t, 0)$  jump while rotating  $\vec{B}_0$  for an angle of  $\beta_x = 2.36^\circ$  with  $\phi = 0^\circ$ . The blue line shows the phase before rotation and during transition process determined by low-pass filter characteristics of the lock-in amplifier. The line in darker green presents decaying phase after filter of the lock-in has settled. The red dashed line shows the fit to the data in darker green according to Eq. 53. The fit function is extrapolated to  $t = 0$  (green point) to obtain  $\varphi_x(0, 0)$ . The vertical dashed line at  $t = 0$  marks the moment when the rotation happens. The horizontal dashed line marks the value of  $\varphi \approx \pi/2$  after the transient process has ended. From the fit, we estimate  $\gamma_{\text{tot}} = 2\pi 4.3(3)$  rad/s and  $a_x = -6.04(15)^\circ$ .

## B. Experimental results

As an example, Figure 6 shows the phase  $\varphi_x(t, 0)$  recorded by the lock-in amplifier for  $\beta_x = 2.36^\circ$  and  $\phi = 0$ . The amplitude  $a_x$  is extracted using the fit function

$$\varphi_{x,y}(t, \phi) = -\frac{\pi}{2} + o + a_{x,y}(\phi) e^{-\gamma_{\text{tot}} t}, \quad (53)$$

where  $o$  accounts for an offset due to a small detuning of Larmor frequency,  $a_{x,y}(\phi)$  is the (initial) amplitude of the signal and  $\gamma_{\text{tot}} = 2\pi 4.3(3)$  rad/s is the relaxation rate. The total relaxation rate,  $\gamma_{\text{tot}}$ , later used to compare theoretical prediction and the experimental observations, is estimated as a mean value of multiple fits for various values of  $\phi$  and its uncertainty is inferred from the resulting standard deviation. The fit is performed on data points, labeled by green color in Fig. 6. The blue data points contain the transient of the lock-in's low pass filter and state of the magnetometer before the rotation.

We perform a series of such measurements for different  $\phi$  and  $\beta_{x,y} = -1.33^\circ$ . Figure 7 shows the experimental result (points), together with theoretical prediction (solid lines), where we use the fit function

$$\varphi_{x,y}(0, \phi) = -\frac{\pi}{2} + \theta_{x,y} + \beta_{x,y} C_{x,y} \sin(\phi + \phi_{\text{sh}}). \quad (54)$$

In Fig. 7, the red color denotes the rotation around the  $x$ -axis, and blue rotation around the  $y$ -axis. The prediction given by Eqs. 47 and 48 is confirmed. The small discrepancy could be explained by the performed approximations, a possible misalignment of the magnetometer

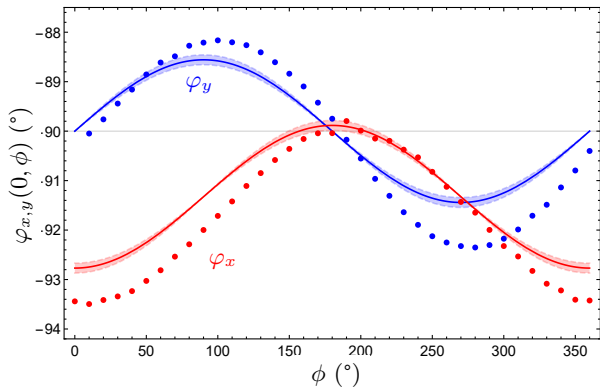


FIG. 7. Comparison of theoretical prediction with experimental observations of the dependence of the initial phase jump amplitude on the rf field phase. Dots represent  $\varphi_{x,y}(0, \phi)$  extracted by fit of Eq. 53 and solid lines theoretical prediction for rotation of  $\vec{B}_0$  around  $x$ - (red) and  $y$ -axis (blue). Theoretical line is generated with  $\beta_{x,y} = -1.33^\circ$ ,  $\gamma_{\text{tot}} = 2\pi 4.3(3)$  rad/s and  $G_{\text{rf}} = 2\pi 3.96$  rad/s. The shaded area around lines shows the uncertainty range due estimation error of  $\gamma_{\text{tot}}$ .

with respect to the field coils and by phase delays and shifts induced by the electrical circuitry.

We performed three sets of measurements  $\beta \in \{-0.66^\circ, -1.33^\circ, -2.36^\circ\}$  for different  $\phi$  as described above and shown in Fig. 7. We use the fit function Eq. 54 to extract values for  $\theta_{x,y}$  and  $C_{x,y} = \gamma_{\text{tot}}/G_{\text{rf}}$ . Please note that, according to Eq. 50, the  $\theta_y$  should be zero, but the experimental data show otherwise. The fit parameter  $\phi_{\text{sh}}$  accounts for a small phase shift and for transformation of sin to cos.

In Figure 8 we show the extracted values of  $\theta_{x,y}$  as a function of  $\beta_{x,y}$ . As  $\alpha = \pi/2$  in our experiment,  $\theta_x = \beta_x$  (presented as solid black line), according to Eq. 43. In Fig. 8, the dots are results extracted by the fit and the dashed lines represent linear regressions. Both  $\theta_{x,y}$  are close to theoretical prediction. We assume the small deviation to be due to mechanical misalignment of the magnetometer with respect to the field coils on the order of a few degrees.

Figure 9 shows the dependence of  $\beta_{x,y} C_{x,y}$  on  $\beta_{x,y}$ . In this figure, the dots result from a fit by Eq. 54 and the dashed lines represent linear regressions. The solid black line, with shaded area is the expected value  $\beta_{x,y} C_{x,y}$  with error due uncertainty of  $\gamma_{\text{tot}} = 2\pi 4.3(3)$  rad/s.

#### IV. DISCUSSION

The DPPE can solely be explained from classical Bloch spin dynamics and is not related with other known phenomena leading to orientational dependence of nominally scalar OPM readout, like 'classical' heading errors arising from nonlinear Zeeman splitting, (vector) light shifts, channel balancing in differential schemes, or dead zones as recently discussed, e.g. in [36]. While 'classical' head-

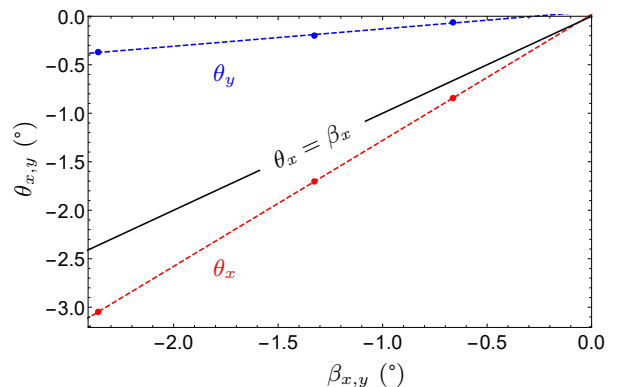


FIG. 8. Values of  $\theta_{x,y}$  extracted by fit according to Eq. 54. The dots are results of the fit, the dashed lines are linear regressions and the black solid line marks the expectation  $\theta_x = \beta_x$  as  $\alpha = 45^\circ$ , according to Eq. 43.

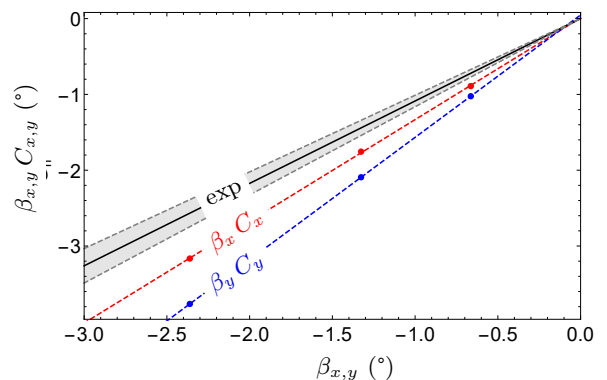


FIG. 9. Extracted values of  $\beta_{x,y} C_{x,y}$  by fit function Eq. 54. The dots are results of the fit, dashed lines are linear regressions and the black solid line presents the expected (exp) result for  $\alpha = 45^\circ$ ,  $\gamma_{\text{tot}} = 2\pi 4.3(3)$  rad/s and  $G_{\text{rf}} = 2\pi 3.96$  rad/s. The shaded area marks the error due to uncertainty of fitted  $\gamma_{\text{tot}}$ .

ing errors increase with increasing magnetic field modulus, the DPPE amplitude depends on tilting angle  $\beta$ , which, to first order is  $\propto B_{\perp}/B_0$ . Thus, the effect cannot be mitigated by restriction to low magnetic fields.

Inspection of Eqs. 47-50 shows the strong dependence of DPPE amplitude and transient duration on the total relaxation rate  $\gamma_{\text{tot}}$  and strength of  $B_{\text{rf}}$  (i.e.  $G_{\text{rf}}$ ). As seen from Eqs. 45 and 46, DPPE scales with  $\gamma_p$ , thus in low-power regime, linear with light intensity. This makes the behaviour similar, but unrelated to (AC Stark) light shift phenomena. However, for DPPE the light does not need to be spectrally detuned.

One strategy to avoid DPPE is to restrict to applications where the variations of the magnetic field vector are in parallel to  $\vec{B}_0$ . Another strategy could be to have magnetic field variations only in direction of  $x$ -axis (rotation around  $y$ ) and use averaging of many randomly timed samples, relying on Eq. 52 to suppress DPPE by averaging over random  $\phi$ .

In the case for rotation around the  $x$ -axis one can esti-

mate the required pointing stability of the magnetic field to have the DPPE below typical noise and accuracy figures of an  $M_x$  magnetometer:

For our  $^{133}\text{Cs}$  magnetometer with a total relaxation rate of  $\gamma_{\text{tot}} = 2\pi 4.3$  rad/s (as measured), the slope of the phase signal at its symmetry point is  $\Delta\varphi/\Delta B = \gamma_F/\gamma_{\text{tot}} = 0.81$  rad/nT (cp. Eq. 1). This means, that a 1 pT field change in  $|\vec{B}_0|$  corresponds to a change in phase signal of  $\Delta\varphi = 46$  mdeg.

With  $G_{\text{rf}} = 2\pi 3.96$  rad/s, and  $\alpha = 45^\circ$ , according to Eq. 47 to get an error due to DPPE of  $\Delta\varphi = 46$  mdeg at  $t = 0$ , the required tipping angle  $\beta$  is only 21 mdeg. In other words, with DPPE,  $\vec{B}_0$  tipping angles of  $\beta = 0.0021^\circ$  ( $\beta = 0.00021^\circ$ ) around the  $x$ -axis will lead to transient readout errors resembling effective magnetic field changes of 100 fT (10 fT) in the phase signal of our magnetometer. Obtaining a magnetic field pointing stability on this level represents a challenging technical task even in very well magnetically shielded environment.

This result gains further relevance when seen in the context of, e.g., technical noise sources like magnetic field interference from power lines (50/60 Hz and harmonics). The direction of those fields with respect to the static magnetic field is very rarely known, nor well under control. For example, an interference field component of  $\vec{B}_{\text{IF}} = 18.3$  nT perpendicular to the geomagnetic field vector ( $|\vec{B}_0| = 50 \mu\text{T}$  assumed here) would be sufficient to generate a 1 pT amplitude DPPE. This is on the order of values which are typically observed in a magnetically calm lab or field environment.

When the magnetometer is operated in free-running mode (cp. Sec. I), the phase signal will show excursions that mimic changes of the static magnetic field modulus. Beyond that, when a PLL is active with sufficiently large bandwidth to cover the DPPE dynamics, the feedback will lead to erroneous control of  $\omega_{\text{rf}}$ . This will inflict additional noise in the sensor readout and can represent an obstacle to increasing the sensor bandwidth by increasing the PLL bandwidth. To obtain measurements undisturbed from DPPE, the magnetometer needs to be allowed to settle into its steady state, assuming that the magnetic field tilts are on a much slower time scale than the DPPE response. However, in this case, as the response time is inversely coupled to the relaxation rate  $\gamma_{\text{tot}}$  (typically minimized to obtain high sensitivity), this time scale can be very long, severely limiting the sensor bandwidth.

This limitation to bandwidth represents a strong obstacle in applications where the sensor shall be moved within the magnetic field, in particular when used on a moving platform within the geomagnetic field.

DPPE is not restricted to single-beam  $M_x$  magnetometers, nor to schemes, where a change in transmitted light intensity is detected. Moreover, we expect it to be relevant in any configuration where rf magnetic fields are used to coherently drive the spin precession of a spin-

polarized ensemble, and a phase-sensitive read-out is employed. This includes more sophisticated OPM pump-probe schemes, detection of nonlinear magneto-optical or Faraday rotation [1]. The effect is not restricted to thermal vapors, it could also be seen in other rf- or microwave-driven spin-polarized systems, e.g., ultracold atoms [37], liquids or solid-state systems.

## V. CONCLUSION

We have investigated the demodulation phase signal response in rf-driven optically pumped magnetometers. The dependence of the static phase offset on the direction of the magnetic field vector with respect to the sensor orientation, as seen in classical  $M_x$  magnetometers, can be largely overcome by aligning rf field oscillation and light propagation direction (TSM). However, while the static phase projection error (SPPE) is largely absent in the TSM configuration, we show that even in this scheme a transient phase signal can arise from tilts of the static magnetic field with respect to the sensor orientation (DPPE). We obtain analytical results solving the modified Bloch equation which are in agreement with our measurements using an  $M_x$  magnetometer employing a  $^{133}\text{Cs}$  paraffin-coated vapor cell. We discuss the importance of the effect in practical applications due to its consequences regarding the static magnetic field pointing stability and implications on sensor bandwidth. The results highlight fundamental limitations of rf-driven implementations of optically pumped magnetometers, which, albeit their wide-spread use in research, have not been discussed in literature to date. Alternative approaches, based on the observation of free spin precession, as presented, e.g., in [38–41], are not suffering from DPPE, thus turn out to be beneficial with respect to accuracy and rotation invariance of measurement in this regard. In our opinion, this, besides technical advances in the required sensor control and read-out electronics, presents a valid reason for the renewed interest in these alternative types of pulsed OPMs.

## ACKNOWLEDGMENTS

M. Č., A. K., Z. G., and T. S. acknowledge support received within the project "free alignment precession optically pumped magnetometer (FRAPOPm)" funded by the German Federal Ministry of Education and Research (BMBF) under the grant number 01DS21006. M. Č., A. K., Z. G. acknowledge funding provided by the Institute of Physics Belgrade through a grant by the Ministry of Education, Science and Technological Development of the Republic of Serbia. T. S. acknowledges support within the project Rio-GNOME funded by the German research foundation (DFG) under grant number 439720477.

- [1] D. Budker and D. F. Jackson Kimball, eds., *Optical magnetometry* (Cambridge University Press, 2013).
- [2] G. Bison, N. Castagna, A. Hofer, P. Knowles, J.-L. Schenker, M. Kasprzak, H. Saudan, and A. Weis, *Applied Physics Letters* **95**, 173701 (2009).
- [3] S. Morales, M. C. Corsi, W. Fourcault, F. Bertrand, G. Cauffet, C. Gobbo, F. Alcouffe, F. Lenouvel, M. L. Prado, F. Berger, G. Vanzetto, and E. Labyt, *Physics in Medicine & Biology* **62**, 7267 (2017).
- [4] K. Jensen, M. A. Skarsfeldt, H. Stærkind, J. Arnbak, M. V. Balabas, S.-P. Olesen, B. H. Bentzen, and E. S. Polzik, *Scientific Reports* **8**, 16218 (2018).
- [5] Y. Yang, M. Xu, A. Liang, Y. Yin, X. Ma, Y. Gao, and X. Ning, *Scientific Reports* **11**, 5564 (2021).
- [6] E. Boto, N. Holmes, J. Leggett, G. Roberts, V. Shah, S. S. Meyer, L. D. Muñoz, K. J. Mullinger, T. M. Tierney, S. Bestmann, G. R. Barnes, R. Bowtell, and M. J. Brookes, *Nature* **555**, 657 (2018).
- [7] M. J. Brookes, J. Leggett, M. Rea, R. M. Hill, N. Holmes, E. Boto, and R. Bowtell, *Trends in Neurosciences* **45**, 621 (2022).
- [8] S. Afach, B. C. Buchler, D. Budker, C. Dailey, A. Derevianko, V. Dumont, N. L. Figueroa, I. Gerhardt, Z. D. Grujić, H. Guo, C. Hao, P. S. Hamilton, M. Hedges, D. F. Jackson Kimball, D. Kim, S. Khamis, T. Kornack, V. Lebedev, Z.-T. Lu, H. Masia-Roig, M. Monroy, M. Padniuk, C. A. Palm, S. Y. Park, K. V. Paul, A. Penafior, X. Peng, M. Pospelov, R. Preston, S. Pustelny, T. Scholtes, P. C. Segura, Y. K. Semertzidis, D. Sheng, Y. C. Shin, J. A. Smiga, J. E. Stalnaker, I. Sulai, D. Tandon, T. Wang, A. Weis, A. Wickenbrock, T. Wilson, T. Wu, D. Wurm, W. Xiao, Y. Yang, D. Yu, and J. Zhang, *Nature Physics* **17**, 1396 (2021).
- [9] C. Abel, S. Afach, N. J. Ayres, C. A. Baker, G. Ban, G. Bison, K. Bodek, V. Bondar, M. Burghoff, E. Chanel, Z. Chowdhuri, P.-J. Chiu, B. Clement, C. B. Crawford, M. Daum, S. Emmenegger, L. Ferraris-Bouchez, M. Fertl, P. Flaux, B. Franke, A. Fratangelo, P. Geltenbort, K. Green, W. C. Griffith, M. van der Grinten, Z. D. Grujić, P. G. Harris, L. Hayen, W. Heil, R. Henneck, V. Hélaine, N. Hild, Z. Hodge, M. Horras, P. Iaydjiev, S. N. Ivanov, M. Kasprzak, Y. Kermaidic, K. Kirch, A. Knecht, P. Knowles, H.-C. Koch, P. A. Koss, S. Komposch, A. Kozela, A. Kraft, J. Krempel, M. Kuźniak, B. Lauss, T. Lefort, Y. Lemièrre, A. Leredde, P. Mohanmurthy, A. Mtchedlishvili, M. Musgrave, O. Naviliat-Cuncic, D. Pais, F. M. Piegsa, E. Pierre, G. Pignol, C. Plonka-Spehr, P. N. Prashanth, G. Quéméner, M. Rawlik, D. Rebreyend, I. Rienäcker, D. Ries, S. Roccia, G. Rogel, D. Rozpedzik, A. Schnabel, P. Schmidt-Wellenburg, N. Severijns, D. Shiers, R. Tavakoli Dinani, J. A. Thorne, R. Viot, J. Voigt, A. Weis, E. Wursten, G. Wyszynski, J. Zejma, J. Zenner, and G. Zsigmond, *Phys. Rev. Lett.* **124**, 081803 (2020).
- [10] G. Oelsner, R. IJsselsteijn, T. Scholtes, A. Krüger, V. Schultze, G. Seyffert, G. Werner, M. Jäger, A. Chwala, and R. Stolz, *Phys. Rev. Appl.* **17**, 024034 (2022).
- [11] Y. Lu, T. Zhao, W. Zhu, L. Liu, X. Zhuang, G. Fang, and X. Zhang, *Sensors* **23**, 10.3390/s23115318 (2023).
- [12] A. Jauffenthaler, P. Schier, T. Middelmann, M. Liebl, F. Wiekhorst, and D. Baumgarten, *Sensors* **20**, 753 (2020).
- [13] V. Lebedev, A. Jauffenthaler, T. Middelmann, and D. Baumgarten, Unshielded high-bandwidth magnetorelaxometry of magnetic nanoparticles with optically pumped magnetometers, in *Flexible High Performance Magnetic Field Sensors: On-Scalp Magnetoencephalography and Other Applications*, edited by E. Labyt, T. Sander, and R. Wakai (Springer International Publishing, Cham, 2022) pp. 247–265.
- [14] T. Sasayama, S. Taue, and T. Yoshida, *AIP Advances* **14**, 015029 (2024).
- [15] A. Pollinger, C. Amtmann, A. Betzler, B. Cheng, M. Ellmeier, C. Hagen, I. Jernej, R. Lammegger, B. Zhou, and W. Magnes, *Geoscientific Instrumentation, Methods and Data Systems* **9**, 275 (2020).
- [16] C. Schirninger, H. U. Eichelberger, W. Magnes, M. Y. Boudjada, K. Schwingenschuh, A. Pollinger, B. P. Besser, P. F. Biagi, M. Solovieva, J. Wang, B. Cheng, B. Zhou, X. Shen, M. Delva, and R. Lammegger, *Remote Sensing* **13**, 10.3390/rs13122360 (2021).
- [17] C. Deans, T. Valenzuela, and M. Bason, in *International Conference on Space Optics — ICSO 2022*, Vol. 127777, edited by K. Minoglou, N. Karafolas, and B. Cugny, International Society for Optics and Photonics (SPIE, 2023) p. 127776W.
- [18] K.-M. C. Fu, G. Z. Iwata, A. Wickenbrock, and D. Budker, *AVS Quantum Science* **2**, 044702 (2020).
- [19] D. Budker, W. Gawlik, D. F. Kimball, S. M. Rochester, V. V. Yashchuk, and A. Weis, *Rev. Mod. Phys.* **74**, 1153 (2002).
- [20] W. E. Bell and A. L. Bloom, *Phys. Rev.* **107**, 1559 (1957).
- [21] A. L. Bloom, *Appl. Opt.* **1**, 61 (1962).
- [22] E. B. Aleksandrov, M. V. Balabas, A. K. Vershovskii, A. E. Ivanov, N. N. Yakobson, V. L. Velichanskii, and N. V. Senkov, *Rev. Mod. Phys.* **74**, 1153 (2002).
- [23] S. Groeger, G. Bison, J.-L. Schenker, R. Wynands, and A. Weis, *The European Physical Journal D - Atomic, Molecular, Optical and Plasma Physics* **38**, 239 (2006).
- [24] P. D. D. Schwindt, B. Lindseth, S. Knappe, V. Shah, J. Kitching, and L.-A. Liew, *Applied Physics Letters* **90**, 081102 (2007).
- [25] T. Scholtes, V. Schultze, R. IJsselsteijn, S. Woetzel, and H.-G. Meyer, *Phys. Rev. A* **84**, 043416 (2011).
- [26] W. Happer, *Rev. Mod. Phys.* **44**, 169 (1972).
- [27] S. Colombo, V. Dolgovskiy, T. Scholtes, Z. D. Grujić, V. Lebedev, and A. Weis, *Applied Physics B* **123**, 1432 (2017).
- [28] G. Bison, R. Wynands, and A. Weis, *Journal of The Optical Society of America B-optical Physics* **22**, 77 (2004).
- [29] A. Weis, G. Bison, and Z. D. Grujić, Magnetic resonance based atomic magnetometers, in *High Sensitivity Magnetometers*, edited by A. Grosz, M. J. Haji-Sheikh, and S. C. Mukhopadhyay (Springer International Publishing, Cham, 2017) pp. 361–424.
- [30] Electronic (possibly frequency-dependent) phase shifts can arise from rf coil and cable inductance, limited bandwidth of the photo current transimpedance amplifier, etc.
- [31] F. Bloch, *Phys. Rev.* **70**, 460 (1946).
- [32] T. Scholtes, S. Woetzel, R. IJsselsteijn, V. Schultze, and H.-G. Meyer, *Applied Physics B* **117**, 211 (2014).

- [33] Wolfram Research, Inc., Mathematica, Version 13.1 (2022), Champaign, IL.
- [34] Z. D. Grujić and A. Weis, *Phys. Rev. A* **88**, 012508 (2013).
- [35] N. Castagna, G. Bison, G. Di Domenico, A. Hofer, P. Knowles, C. Macchione, H. Saudan, and A. Weis, *Applied Physics B* **96**, 763 (2009).
- [36] G. Oelsner, V. Schultze, R. IJsselsteijn, F. Wittkämper, and R. Stolz, *Phys. Rev. A* **99**, 013420 (2019).
- [37] Y. Cohen, K. Jadeja, S. Sula, M. Venturelli, C. Deans, L. Marmugi, and F. Renzoni, *Applied Physics Letters* **114**, 073505 (2019), [https://pubs.aip.org/aip/apl/article-pdf/doi/10.1063/1.5084004/14522954/073505\\_1.online.pdf](https://pubs.aip.org/aip/apl/article-pdf/doi/10.1063/1.5084004/14522954/073505_1.online.pdf).
- [38] Z. D. Grujić, P. A. Koss, G. Bison, and A. Weis, *Eur. Phys. J. D* **69**, 135 (2015).
- [39] S. Afach, G. Ban, G. Bison, K. Bodek, Z. Chowdhuri, Z. D. Grujić, L. Hayen, V. Hélaine, M. Kasprzak, K. Kirch, P. Knowles, H.-C. Koch, S. Komposch, A. Kozela, J. Krempel, B. Lauss, T. Lefort, Y. Lemièrre, A. Mtchedlishvili, O. Naviliat-Cuncic, F. M. Piegsa, P. N. Prashanth, G. Quémener, M. Rawlik, D. Ries, S. Roccia, D. Rozpedzik, P. Schmidt-Wellenburg, N. Severjins, A. Weis, E. Wursten, G. Wyszynski, J. Zejma, and G. Zsigmond, *Opt. Express* **23**, 22108 (2015).
- [40] D. Hunter, S. Piccolomo, J. D. Pritchard, N. L. Brockie, T. E. Dyer, and E. Riis, *Phys. Rev. Appl.* **10**, 014002 (2018).
- [41] V. Gerginov, M. Pomponio, and S. Knappe, *IEEE Sensors Journal* **20**, 12684 (2020).